Geological Magazine

www.cambridge.org/geo

Mid-Neoproterozoic magmatism in the South Qilian Belt, NE Tibetan Plateau and its tectonic implications

Yu Qin[1,2], Xiaoli Zhang[1], Qiao Feng[3], Xi Zhang[2], Yun Liu[4], Yu Kang[1], Yan Chen[5], Pengju Chu[2], Yuexiang Yang[2], Lingchuan Tian[2] and Longxue Li[2]

[1]State Key Laboratory of Continental Dynamics, Department of Geology, Northwest University, Northern Taibai Str. 229, Xi'an 710069, China; [2]School of Petroleum Engineering and Environmental Engineering, Yan'an University, Yan'an 716000, China; [3]Shandong Provincial Key Laboratory of Depositional Mineralization & Sedimentary Minerals, Shandong University of Science and Technology, Qingdao 266590, China; [4]Geological Exploration Institute of Shandong Zhengyuan, China Metallurgical Geology Bureau, Ji'nan 250014, China and [5]Qinghai Oilfield Branch PetroChina, Dunhuang 736202, China

Original Article

Cite this article: Qin Y, Zhang X, Feng Q, Zhang X, Liu Y, Kang Y, Chen Y, Chu P, Yang Y, Tian L, and Li L (2022) Mid-Neoproterozoic magmatism in the South Qilian Belt, NE Tibetan Plateau and its tectonic implications. *Geological Magazine* **159**: 1384–1396. https://doi.org/10.1017/S001675682200022X

Received: 29 January 2021
Revised: 31 December 2021
Accepted: 5 March 2022
First published online: 30 May 2022

Keywords:
zircon U–Pb–Hf isotopes; whole-rock geochemistry; gabbro; petrogenesis; south qilian belt

Author for correspondence: Xiaoli Zhang, Email zhangxiaoli_nwu@163.com

Abstract

Widely distributed Mid-Neoproterozoic mafic rocks of the Qilian – Qaidam – East Kunlun region record the tectonic evolution of the northeastern Tibetan Plateau. This study presents whole-rock geochemistry, zircon U–Pb geochronology and Hf isotopes for the Xialanuoer gabbros of the central South Qilian Belt (SQB). Zircon laser ablation – inductively coupled plasma – mass spectrometry (LA-ICP-MS) U–Pb dating indicates that the gabbros were emplaced at *ca.* 738 Ma, indicating they are contemporaneous with mafic magmatism elsewhere in the northeastern Tibetan Plateau. The gabbros have low SiO_2, Cr and Ni contents and Mg# values, are relatively enriched in light rare-earth elements (LREEs) and depleted in high-field-strength elements (HFSEs; e.g. Nb and Ta), have no positive Zr or Hf anomalies and have relatively high Nb/Ta but low Nb/La ratios. These data indicate that the Xialanuoer gabbros formed from calc-alkaline basaltic magmas that were originally generated by the partial melting of an enriched mantle of type-I (EMI-type) enriched region of the lithospheric mantle, underwent little to no crustal contamination prior to their emplacement, and have within-plate basalt geochemical affinities. Combining these data with the presence of widespread contemporaneous continental rift-related magmatism and sedimentation in the North Qilian, Central Qilian, South Qilian, Quanji, North Qaidam and East Kunlun regions suggests that the northeastern Tibetan Plateau underwent Mid-Neoproterozoic continental rifting, which also affected other Rodinian blocks (e.g. Tarim, South China, Australia, North America and Southern Africa).

1. Introduction

The Rodinia supercontinent was assembled between 1.3 and 0.9 Ga, before breaking up between 850 and 740 Ma (Li *et al.* 2008). Several blocks that were formerly part of Rodinia record multiple episodes of anorogenic magmatism at 850–740 Ma, including South China, Tarim, North America, India, Southern Africa and Australia (Powell *et al.* 1994; Park *et al.* 1995; Preiss, 2000; Frimmel *et al.* 2001; Ling *et al.* 2003; Li *et al.* 2008; Wang *et al.* 2011; Xu *et al.* 2013; Zhang *et al.* 2013; McClellan & Gazel, 2014; Wan *et al.* 2019).

The Qilian Orogen in the northeastern Tibetan Plateau is an important part of the Qin–Qi–Kun Central China Orogenic System. It is bordered by the North China Craton to the northeast, the South China Craton to the southeast and the Tarim Craton to the northwest (Fig. 1a) (Xiao *et al.* 2009; Song *et al.* 2013). The orogen is subdivided into the South Qilian Belt (SQB), Central Qilian Block and North Qilian Belt, with the SQB thought to preserve evidence of 786–713 Ma magmatism (Ma *et al.* 2017; Bai *et al.* 2019; Wang *et al.* 2019; Ji *et al.* 2020). However, the petrogenesis and tectonic setting of this magmatism remain unclear, with two contrasting models proposed to explain these events to date. The first of these suggests that magmatism occurred in a continental rift setting as a result of mantle plume activity associated with the final break-up of Rodinia (Bai *et al.* 2019; Ji *et al.* 2020). The second model suggests that magmatism occurred in arc-type tectonic settings (Ma *et al.* 2017; Wang *et al.* 2019). Further research is needed to precisely constrain the geochemical characteristics and affinities of these magmatic events, and their geodynamic setting.

This study presents new zircon U–Pb–Hf isotopic and whole-rock geochemical data for the Xialanuoer gabbros of the central SQB. Combining these new data with the results of previous research allows the Mid-Neoproterozoic tectonic setting of the SQB to be better constrained, and provides insights into the Mid-Neoproterozoic tectonic evolution of the Qilian – Qaidam – East Kunlun region of the northeastern Tibetan Plateau.

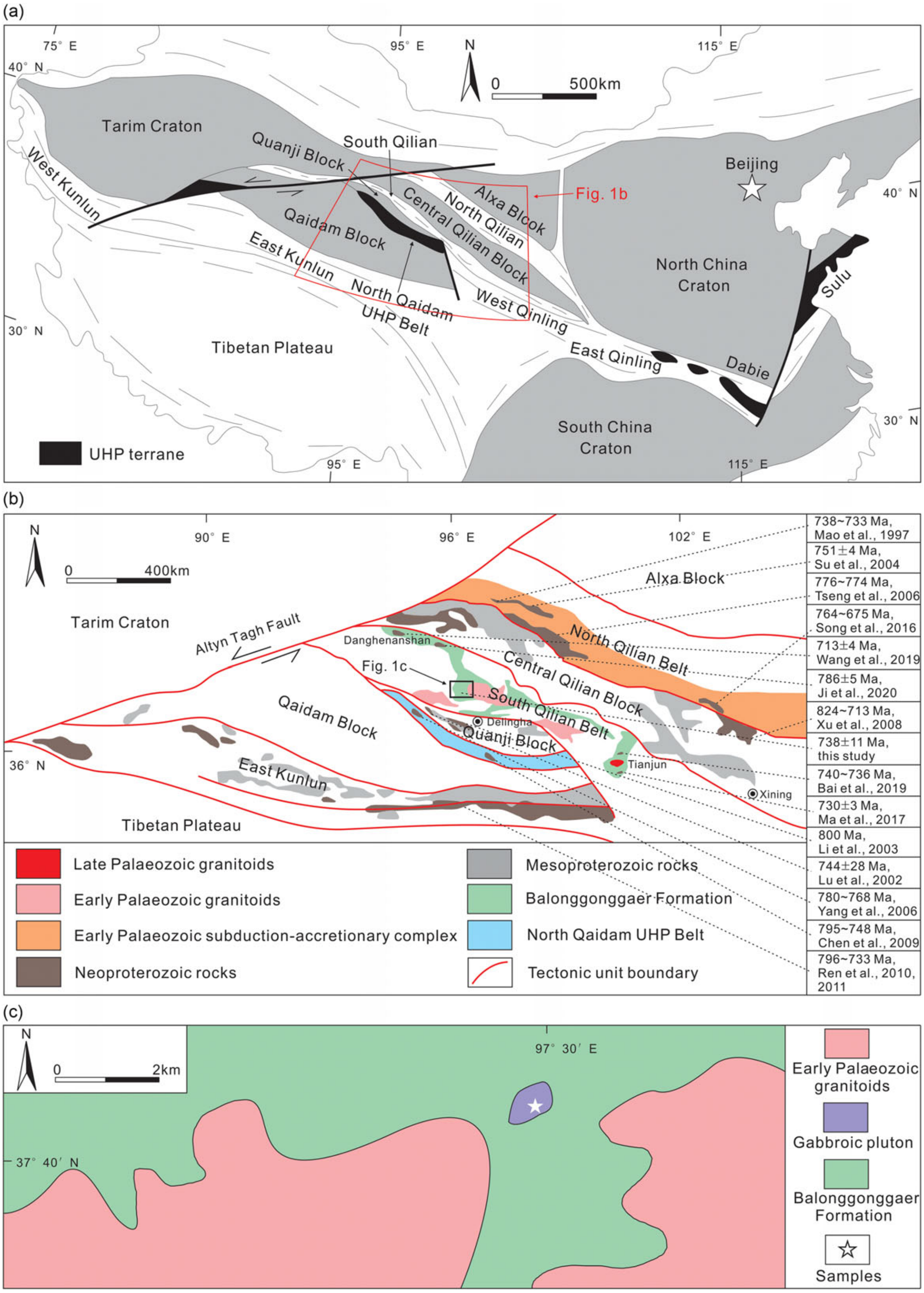

Fig. 1. (Colour online) (a) Tectonic framework of China and location of the study area (modified after Song *et al.* 2013). (b) Tectonic subdivision of the northeastern Tibetan Plateau, showing the tectonic location of the SQB (modified after Lu *et al.* 2008). Igneous rocks age data sources: 738–733 Ma (Mao *et al.* 1997); 751 ± 4 Ma (Su *et al.* 2004); 776–774 Ma (Tseng *et al.* 2006); 764–675 Ma (Song *et al.* 2016); 713 ± 4 Ma (Wang *et al.* 2019); 786 ± 5 Ma (Ji *et al.* 2020); 824–713 Ma (Xu *et al.* 2008); 738 ± 11 Ma (this study); 740–736 Ma (Bai *et al.* 2019); 730 ± 3 Ma (Ma *et al.* 2017); 800 Ma (Li *et al.* 2003); 744 ± 28 Ma (Lu *et al.* 2002); 780–768 Ma (Yang *et al.* 2006); 795–748 Ma (Chen *et al.* 2009); 796 ± 41 Ma (Ren *et al.* 2011); 733 ± 6 Ma (Ren *et al.* 2010). (c) Geological map of the Xialanuoer area (modified after Qin, 2018) showing sample locality.

2. Geological background

The Qilian Orogen is bounded by the Altyn fault to the northwest, extends to the east into the Qinling Orogen, and borders the Quanji and Alxa blocks to the south and north, respectively (Fig. 1b).

The North Qilian Belt represents a subduction-related accretionary complex formed by the Palaeozoic closure of the Proto-Tethys North Qilian Ocean between the Alxa and Central Qilian blocks (Xia *et al.* 2016; Wang *et al.* 2017; Peng *et al.* 2019). It comprises Neoproterozoic to Early Palaeozoic ophiolite sequences, high-pressure (HP) metamorphic belts, island arc volcanic rocks and granitoid plutons, Silurian flysch and Devonian molasse deposits, and Carboniferous to Triassic sedimentary cover sequences (Yang *et al.* 2009; Xu *et al.* 2010; Yu *et al.* 2015; Qin *et al.* 2021).

The Central Qilian Block is a Precambrian microcontinent comprising Meso–Neoproterozoic greenschist- to amphibolite-facies metasedimentary rocks, metamorphosed plutons and dolomitic marbles, all of which are covered by Palaeozoic sedimentary sequences (Hou *et al.* 2005; Xu *et al.* 2007; Tung *et al.* 2013).

The SQB is dominated by the Neoproterozoic–early Paleozoic tectonic melange (Balonggonggaer Formation), which comprises mainly schists and greywackes (Ji *et al.* 2018; Qin, 2018; Li *et al.* 2019). Although the maximum depositional age of the schists in the Balonggonggaer Formation is constrained by the youngest detrital zircon U–Pb age peaks at 824–720 Ma (Li *et al.* 2019; Qin, 2018), the existence of older rocks can't be ruled out. Moreover, the belt contains small volumes of locally exposed Mid-Neoproterozoic magmatic rocks that are dominated by 786–713 Ma basalts and gabbros (Ma *et al.* 2017; Bai *et al.* 2019; Wang *et al.* 2019; Ji *et al.* 2020). The SQB also contains voluminous Palaeozoic (457–418 Ma) granitoids associated with minor volcanic rocks (Liao *et al.* 2014; Niu *et al.* 2016; Zhang *et al.* 2016; DL Li *et al.* 2018*a*) that formed as a result of the early Palaeozoic closure of the Proto-Tethys South Qilian Ocean (Fu *et al.* 2018; Yan *et al.* 2019).

3. Sample descriptions

This study focuses on a gabbroic pluton that crops out ~80 km northwest of Delingha in the central SQB in the Xialanuoer area. The pluton is relatively small (1 km × 0.5 km) and elliptical and preserved in the Balonggonggaer Formation (Fig. 1c). A total of seven samples (DLH-1 to 7) were collected from the gabbroic pluton; details of sampling locations and mineral assemblages are provided in Table 1. All of the samples are metagabbro with medium- to fine-grained granular textures and massive structures. They are composed of olivine (10–20 %), clinopyroxene (40–50 %), plagioclase (35–45 %) and minor minerals of sphene and chlorite. Granular olivine and subhedral plagioclase are included in subhedral clinopyroxene (Fig. 2), suggesting the earlier crystallization of olivine and plagioclase. Clinopyroxene edges are often fragmented and, although the gabbros have undergone greenschist-facies metamorphism, they retain clear primary magmatic textures.

Table 1. Summary of the sample locality, lithology and mineral assemblage for the Mid-Neoproterozoic gabbros in the Xialanuoer area

Sample no.	Latitude (° N)	Longitude (° E)	Lithology	Mineral assemblages
DLH-1	37° 53′ 49″	97°27′08″	Gabbro	ol 15 %, cpx 45 %, pl 40 %
DLH-2	37° 54′ 07″	97° 26′ 55″	Gabbro	ol 12 %, cpx 43 %, pl 45 %
DLH-3	37° 53′ 44″	97° 27′ 07″	Gabbro	ol 10 %, cpx 45 %, pl 45 %
DLH-4	37° 53′ 47″	97° 27′ 02″	Gabbro	ol 16 %, cpx 44 %, pl 40 %
DLH-5	37° 53′ 41″	97° 26′ 52″	Gabbro	ol 20 %, cpx 40 %, pl 40 %
DLH-6	37° 54′ 03″	97° 26′ 50″	Gabbro	ol 18 %, cpx 47 %, pl 35 %
DLH-7	37° 53′ 55″	97° 26′ 50″	Gabbro	ol 15 %, cpx 40 %, pl 45 %

4. Analytical methods

All of the analyses were undertaken at the State Key Laboratory of Continental Dynamics of Northwest University, Xi'an, China. Zircon grains were extracted from gabbro samples using standard separation methods before hand-picking under a binocular microscope. These zircon grains were mounted in epoxy resin before polishing to expose zircon interiors. The zircon grains were then imaged using reflected and transmitted light optical microscopy and cathodoluminescence (CL) using a Gatan MonoCL3 CL instrument coupled with a scanning electron microscope.

In situ U–Pb dating was performed using laser ablation – inductively coupled plasma – mass spectrometry (LA-ICP-MS) employing a MicroLasTM Beam Delivery Systems Analyte Excite 193 nm ArF excimer LA system coupled to a Perkin Elmer/SCIEX Elan 6100 ICP-MS instrument. The ablated materials were delivered to the torch in the ICP-MS by high-purity helium gas to ensure efficient aerosol transport. A NIST 610 silicate glass standard was used to tune the ICP-MS to ensure maximum signal sensitivity for high masses (Pb, Th, U; better than 2000 cps μg^{-1} g^{-1}). The analysis used a beam diameter of 32 μm and a laser frequency of 6 Hz, and the NIST 610 U^+ and Th^+ ion-signal intensity ratio (using ^{238}U and $^{232}Th \approx 1$) was used as an indicator of complete vaporization (Günther & Hattendorf, 2005), with oxide formation monitored using ThO^+/Th^+ (<0.5 %). Laser ablation employed time-resolved analysis using single laser spots, with the analysed elements acquired using a peak jumping mode. Dwell times were 10 ms for Th, 15 ms for U, Pb and Ti, and 6 ms for all other elements. Dual-pulse and analogue counting detector modes were automatically converted according to intensity during analysis with pulse/analogue (P/A) factors for each element auto-tuned to ensure best accuracy and efficiency prior to routine analysis. $^{207}Pb/^{206}Pb$, $^{206}Pb/^{238}U$, $^{207}Pb/^{235}U$ and $^{208}Pb/^{232}Th$ ratios were calculated using the GEMOC-developed GLITTER 4.0 software package from Macquarie University, with integrated ratio drift during individual runs corrected to remove both instrumental mass bias and depth-dependent elemental and isotopic fractionations by calibration against a matrix-matched Harvard zircon 91500 standard analysed using the same operating conditions (Wiedenbeck *et al.* 1995). GJ-1 is also a standard sample with a recommended $^{206}Pb/^{238}U$ isotopic age of 603.2 ± 2.4 Ma (XM Liu *et al.* 2007). The concentrations of U, Th, Pb and other trace elements were calibrated using ^{29}Si as an internal standard and the NIST 610 standard as an external standard. The ages were calculated using ISOPLOT/Excel version 4.15 (Ludwig, 2003). The common Pb correction was carried out using the Excel program ComPbCorr#3 (Andersen, 2002). Age uncertainties are quoted at the 95 % confidence level.

Zircon Lu–Hf isotopic compositions were obtained by laser ablation – multicollector – ICP-MS (LA-MC-ICP-MS) employing

Fig. 2. (Colour online) Photographs and photomicrographs of the Mid-Neoproterozoic gabbros from the Xialanuoer area. ol = olivine; pl = plagioclase; cpx = clinopyroxene.

a Nu Plasma HR instrument coupled to a GeoLas 2005 193 nm ArF excimer LA system. This analysis used an applied energy density of 15–20 J cm^{-2}, a laser pulse repetition rate of 8 Hz, and a beam diameter of 44 μm. High-purity helium gas was used as carrier gas to transport ablated particles from the sample chamber to the MC-ICP-MS instrument. Masses of ^{172}Yb, ^{173}Yb, ^{175}Lu, ^{176}(Hf + Yb + Lu), ^{177}Hf, ^{178}Hf, ^{179}Hf and ^{180}Hf were collected simultaneously by Faraday cups with the isobaric interference of ^{176}Lu on ^{176}Hf corrected by measuring the intensity of the interference-free ^{175}Lu isotope and using the recommended ^{176}Lu/^{175}Lu ratio of 0.02669 to calculate ^{176}Lu/^{177}Hf values. The interference of ^{176}Yb on ^{176}Hf was similarly corrected by measuring an interference-free ^{172}Yb isotope and using a ^{176}Yb/^{172}Yb ratio of 0.5886 to calculate corrected ^{176}Hf/^{177}Hf ratios (Chu *et al.* 2002). Measured ^{176}Hf/^{177}Hf ratios were normalized to ^{179}Hf/^{177}Hf = 0.7325. Data quality was assessed by the alternating analysis of 91500 and GJ-1 standard zircon grains as unknowns yielding ^{176}Hf/^{177}Hf ratios of 0.282304 ± 0.000026 ($n = 14$, 2σ) for 91500 and 0.282013 ± 0.000016 ($n = 16$, 2σ) for GJ-1, both of which are consistent and within the uncertainties of the recommended ^{176}Hf/^{177}Hf ratios for these standards (Wu *et al.* 2006). The resulting data were reduced using a ^{176}Lu decay constant of 1.867 × 10^{-11} yr^{-1} (Albarède *et al.* 2006). Present-day ^{176}Hf/^{177}Hf = 0.282785 and ^{176}Lu/^{177}Hf = 0.0336 chondritic values (Bouvier *et al.* 2008) were used to calculate $\epsilon_{\mathrm{Hf}}(t)$ values with single-stage Hf model ages (T_{DM}) calculated relative to the depleted mantle using present-day ^{176}Hf/^{177}Hf and ^{176}Lu/^{177}Hf values of 0.28325 and 0.0384, respectively (Griffin *et al.* 2000). Two-stage model ages ($T^{\mathrm{C}}_{\mathrm{DM}}$) were calculated by projecting initial zircon ^{176}Hf/^{177}Hf ratios back to the depleted mantle growth curve using a value of ^{176}Lu/^{177}Hf = 0.015 for the average continental crust (Griffin *et al.* 2002).

Whole-rock geochemical analysis used fresh whole-rock samples that were trimmed to remove weathered surfaces, cleaned with deionized water, crushed, and finally milled using a tungsten carbide ball mill to pass a ~200 mesh. Major and trace element concentrations were determined by X-ray fluorescence spectrometry (XRF) employing a Rikagu RIX 2100 instrument and ICP-MS employing an Agilent 7500a instrument, respectively. Analyses of United States Geological Survey BHVO-1, AGV-1 and BCR-2 standards yielded analytical precision and accuracy values that are better than 5 % and 10 % for major and trace elements, respectively (Y Liu *et al.* 2007).

5. Results

5.a. Zircon LA-ICP-MS U–Pb dating

A total of 27 zircon grains from gabbro sample DLH-1 were analysed, 13 of which were concordant (90–110 %) and are reported in Table 2. The zircon grains are prismatic with aspect ratios of ~2:1 (Fig. 3). The majority have slight to dark CL luminescence along with internal textures dominated by grown zoning and high Th/U ratios (0.44–2.7) (Table 2; Fig. 3), all of which are indicative of a magmatic origin (Rubatto, 2002; Corfu *et al.* 2003). Nine analyses with concordant ^{206}Pb/^{238}U ages of 757 to 720 Ma yield a weighted average ^{206}Pb/^{238}U age of 738 ± 11 Ma (MSWD = 2.6, $n = 9$) that represents the timing of crystallization of the gabbros. A further four captured zircon grains yield older ages of 2397 to 1295 Ma (Table 2; Fig. 3).

5.b. Whole-rock major and trace element compositions

The major and trace element concentrations of the six representative gabbro samples analysed in this study (DLH-2 to 7) are given in Table 3. These samples have slightly high loss-on-ignition (LOI) values (0.86–1.13 wt %), so major element concentrations were recalculated to 100 % volatile-free totals. The Xialanuoer gabbros contain 45.50–50.18 wt % SiO_2 and heterogeneous Al_2O_3 (14.46–16.85 wt %), Fe_2O_3t (11.14–15.83 wt %), MgO (7.37–10.47 wt %), CaO (7.71–9.09 wt %), TiO_2 (1.68–2.00 wt %), Na_2O (2.43–4.12 wt %) and K_2O (0.75–0.93 wt %) contents. They are metaluminous with A/CNK ratios of 0.71–0.75. They also have a rather restricted range of Mg$^{\#}$ values (56–58). Owing to the potential mobility of large-ion lithophile elements (LILEs; e.g. K, Na, Rb, Sr, Ba and Cs), the samples were classified with respect to immobile elements such as high-field-strength elements (HFSEs) and rare-earth elements (REEs). The majority of the gabbros are classified as subalkaline basalt (barring two samples classified as andesite or basalt) in a Nb/Y vs Zr/TiO_2 classification diagram, consistent with the compositions of contemporaneous mafic rocks in the SQB (Fig. 4a). The Xialanuoer gabbros and contemporaneous mafic rocks are both classified as calc-alkaline and basaltic in a Ta/Yb vs Ce/Yb diagram (Fig. 4b).

The Xialanuoer gabbros have relatively low total REE contents (ΣREE = 61.94–111.19 ppm), have chondrite-normalized REE patterns that are enriched in light REEs (LREEs; 51.34–93.13 ppm) relative to heavy REEs (LREE/HREE = 4.49–5.16, La_N/Yb_N = 4.56–5.27) and have no significant Eu anomalies (Eu/Eu* = 0.97–1.03) (Fig. 5a). The Xialanuoer gabbros are also slightly depleted in REEs relative to contemporaneous mafic rocks in the SQB. They also have primitive-mantle-normalized multi-element variation diagram patterns that are enriched in LILEs (i.e. Rb, Ba and K) and depleted in HFSEs (i.e. Nb and Ta) (Fig. 5b).

5.c. Zircon Hf isotope compositions

The results of zircon Hf isotope analysis are given in Table 4 and shown in Figure 6. The 757–720 Ma zircon grains from sample DLH-1 have very negative $\epsilon_{\mathrm{Hf}}(t)$ values (−13.8 to −6.2), and old

https://doi.org/10.1017/S001675682200022X Published online by Cambridge University Press

Table 2. LA-ICP-MS zircon U–Pb dating results for zircon grains from the Xialanuoer gabbros

		Isotopic ratios						Age (Ma)					
Spot	Th/U	$^{207}Pb/^{206}Pb$	1σ	$^{207}Pb/^{235}U$	1σ	$^{206}Pb/^{238}U$	1σ	$^{207}Pb/^{206}Pb$	1σ	$^{207}Pb/^{235}U$	1σ	$^{206}Pb/^{238}U$	1σ
DLH-1-1	1.09	0.06389	0.00297	1.06823	0.04539	0.12126	0.00196	738	62	738	22	738	11
DLH-1-2	1.58	0.06381	0.00220	1.05489	0.03115	0.11990	0.00162	735	40	731	15	730	9
DLH-1-3	0.98	0.06362	0.00237	1.04508	0.03411	0.11911	0.00169	729	45	726	17	725	10
DLH-1-4	0.65	0.11950	0.00251	5.82433	0.07358	0.35340	0.00403	1949	10	1950	11	1951	19
DLH-1-5	0.99	0.06424	0.00155	1.10140	0.01881	0.12431	0.00145	750	18	754	9	755	8
DLH-1-6	1.90	0.06456	0.00165	1.10985	0.02132	0.12465	0.00148	760	22	758	10	757	8
DLH-1-7	1.79	0.06430	0.00169	1.08684	0.02185	0.12257	0.00147	752	23	747	11	745	8
DLH-1-8	1.57	0.06361	0.00153	1.03690	0.01786	0.11820	0.00138	729	18	722	9	720	8
DLH-1-9	0.44	0.08410	0.00215	2.56778	0.04843	0.22143	0.00271	1295	19	1292	14	1289	14
DLH-1-10	0.57	0.12852	0.00284	6.74799	0.09571	0.38075	0.00447	2078	11	2079	13	2080	21
DLH-1-11	0.48	0.15455	0.00329	9.60399	0.12611	0.45054	0.00520	2397	10	2398	12	2398	23
DLH-1-12	1.92	0.06380	0.00391	1.05617	0.06128	0.12001	0.00239	735	89	732	30	731	14
DLH-1-13	2.70	0.06347	0.00216	1.04098	0.03034	0.11889	0.00159	724	39	724	15	724	9

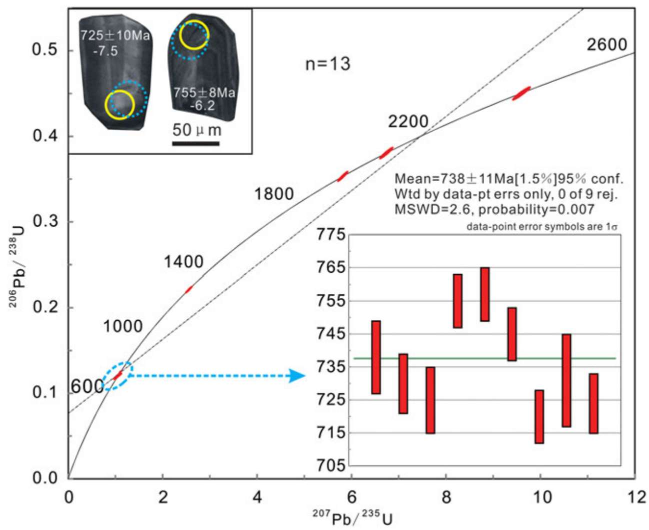

Fig. 3. (Colour online) Representative CL images and U–Pb concordia diagram of zircon grains from the Xialanuoer gabbros. The small yellow and large blue circles are locations for U–Pb dating and Hf-isotope analyses, respectively. Error ellipses represent 1σ uncertainties.

Hf model ages (T_{DM} = 1854–1574 Ma; T^{C}_{DM} = 2498–2046 Ma). The 2078–1295 Ma zircon grains have restricted $\epsilon_{Hf}(t)$ values (−14.7 to −0.7), with older Hf model ages (T_{DM} = 2557–2362 Ma; T^{C}_{DM} = 2985–2620 Ma). However, a 2397 Ma zircon yields a relatively positive $\epsilon_{Hf}(t)$ value of +3.8 and ancient Hf model ages (T_{DM} = 2578 Ma; T^{C}_{DM} = 2690 Ma).

6. Discussion

6.a. Age of the Xialanuoer gabbros and contemporaneous regional magmatism

Due to intense Caledonian tectonism, a large volume of Neoproterozoic igneous rocks that were originally present in this area have been tectonically disrupted and can hardly be recognized. A few Neoproterozoic igneous rocks crop out in the western and eastern SQB, including small volumes of 786–713 Ma basalts (Bai *et al.* 2019; Wang *et al.* 2019; Ji *et al.* 2020) and minor *ca.* 730 Ma gabbros (Ma *et al.* 2017). The Xialanuoer gabbroic pluton is located in the central SQB and preserved in the Balonggonggaer Formation. Previous research has suggested that the pluton was formed during the early Palaeozoic (BGMRQH, 1997), but our new zircon U–Pb dating indicates that the gabbros were actually emplaced at 738 ± 11 Ma. This is contemporaneous with 824–675 Ma magmatism in the North Qilian, Central Qilian, Quanji, North Qaidam and East Kunlun regions of the northeastern Tibetan Plateau, as summarized in Table 5. Although the majority of this mafic magmatism occurred at 796–713 Ma, basalts in the Central Qilian Block suggest that this Mid-Neoproterozoic mafic magmatism began at *ca.* 824 Ma (Xu *et al.* 2008).

6.b. Petrogenesis

The Xialanuoer gabbros have variable but low Ni (108–159 ppm) and Cr (56.5–99 ppm) contents and lower $Mg^{\#}$ values (56–58) (Table 3) than those expected for primary basaltic magmas (Ni > 400 ppm, Cr > 1000 ppm and $Mg^{\#}$ > 73) (Wilson, 1989), suggesting the magmas that formed these gabbros underwent fractional crystallization prior to their emplacement. Moreover, no significant Eu anomalies (Eu/Eu* = 0.97–1.03) are observed, reflecting that the gabbros underwent insignificant fractionation and/or accumulation of plagioclase.

The negative zircon $\epsilon_{Hf}(t)$ values of the *ca.* 738 Ma gabbros (Fig. 6) reflect formation from either melts derived from asthenospheric mantle that underwent crustal contamination prior to emplacement or from an enriched region of the lithospheric mantle. Crustal contamination can significantly affect the geochemical compositions of mafic magmas, causing enrichments in LILEs, Zr and Hf, and depletions in Nb and Ta (Jenner *et al.* 1993). The Xialanuoer gabbros have negative Nb–Ta anomalies but no positive Zr–Hf anomalies (Fig. 5b). Titanium is generally immobile during a variety of geological processes, with negative Ti anomalies often used as evidence of crustal contamination (Bienvenu *et al.* 1990; Rudnick & Gao, 2003). The studied samples have no negative Ti anomalies (Fig. 5b), suggesting that these gabbros record minimal

https://doi.org/10.1017/S0016756822000022X Published online by Cambridge University Press

Table 3. Major- (wt %) and trace-element (ppm) compositions of the Xialanuoer gabbros

Sample	DLH-2	DLH-3	DLH-4	DLH-5	DLH-6	DLH-7
Lithology	Gabbro	Gabbro	Gabbro	Gabbro	Gabbro	Gabbro
SiO_2	44.97	45.25	49.42	49.40	48.51	47.68
TiO_2	1.94	1.98	1.65	1.66	1.73	1.83
Al_2O_3	14.30	14.50	16.06	16.05	16.40	16.62
Fe_2O_3T	15.65	14.90	10.98	10.97	11.22	11.23
MnO	0.22	0.21	0.17	0.17	0.15	0.15
MgO	10.35	9.78	7.66	7.67	7.27	7.28
CaO	7.92	8.21	7.59	7.59	8.43	8.97
Na_2O	2.40	2.50	4.05	4.06	3.80	3.75
K_2O	0.74	0.92	0.74	0.73	0.90	0.92
P_2O_5	0.35	0.38	0.16	0.16	0.19	0.19
LOI	0.86	1.04	1.11	1.13	1.11	1.12
SUM	99.69	99.66	99.60	99.60	99.73	99.74
Li	52.5	50.8	38.2	39.4	33.9	36.1
Be	0.86	0.88	0.64	0.65	0.75	0.77
Sc	26.3	27.2	22.6	22.6	25.6	27.7
V	208	216	197	200	224	243
Cr	99.0	56.5	69.7	70.3	69.7	69.7
Co	78.5	71.6	58.0	58.9	55.4	58.6
Ni	159	125	127	129	108	119
Cu	64.5	41.9	54.4	55.4	52.4	60.4
Zn	113	109	85.5	86.4	86.9	86.0
Ga	17.2	17.6	17.8	17.8	17.7	18.8
Ge	1.42	1.47	1.31	1.34	1.62	1.61
Rb	10.2	13.1	12.4	12.3	15.7	17.8
Sr	263	299	397	396	362	335
Y	25.3	26.9	16.0	16.2	20.2	21.4
Zr	127	144	85.5	86.2	108	112
Nb	4.69	4.93	8.62	8.82	10.8	11.2
Cs	0.40	0.48	0.75	0.75	0.75	0.56
Ba	468	578	1519	1502	657	659
La	15.4	17.7	9.40	9.70	11.3	11.9
Ce	37.0	39.9	22.0	22.2	26.0	28.3
Pr	4.81	5.12	2.78	2.86	3.39	3.66
Nd	21.9	23.5	13.0	13.3	15.8	17.1
Sm	4.89	5.18	3.08	3.18	3.83	4.03
Eu	1.61	1.72	1.08	1.12	1.28	1.34
Gd	4.91	5.16	3.42	3.50	4.14	4.40
Tb	0.76	0.81	0.49	0.53	0.65	0.68
Dy	4.67	4.94	3.03	3.20	3.87	4.05
Ho	0.95	1.00	0.59	0.62	0.75	0.79
Er	2.67	2.80	1.42	1.67	2.05	2.12
Tm	0.38	0.40	0.20	0.23	0.28	0.29

(*Continued*)

https://doi.org/10.1017/S001675682200022X Published online by Cambridge University Press

Table 3. (*Continued*)

Sample	DLH-2	DLH-3	DLH-4	DLH-5	DLH-6	DLH-7
Lithology	Gabbro	Gabbro	Gabbro	Gabbro	Gabbro	Gabbro
Yb	2.42	2.57	1.28	1.39	1.71	1.78
Lu	0.36	0.39	0.17	0.20	0.24	0.26
Hf	3.10	3.46	2.18	2.17	2.68	2.83
Ta	0.28	0.30	0.57	0.57	0.70	0.73
Pb	4.01	3.89	4.10	4.07	1.69	1.56
Th	0.74	0.82	0.95	0.95	1.19	1.25
U	0.17	0.19	0.23	0.23	0.30	0.31

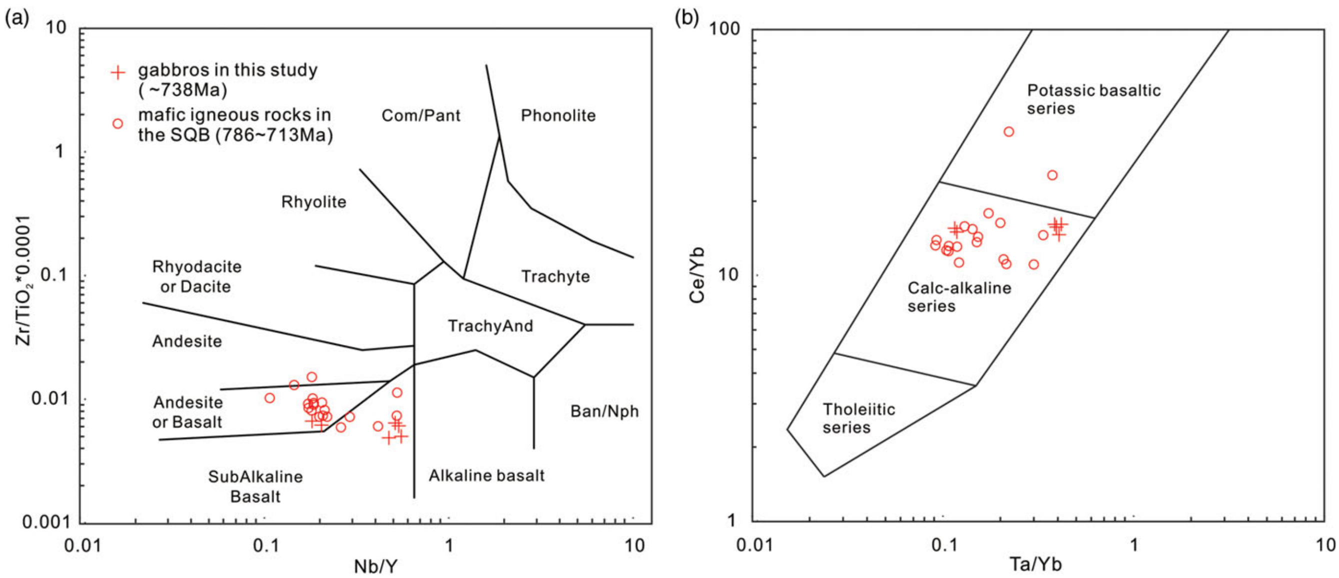

Fig. 4. (Colour online) Rock classification diagrams for the mafic rock samples. (a) Nb/Y vs Zr/TiO$_2$ diagram (Winchester & Floyd, 1977). (b) Ta/Yb vs Ce/Yb diagram (Pearce, 1982). Mid-Neoproterozoic mafic igneous rocks from the SQB (Ma *et al.* 2017; Bai *et al.* 2019; Wang *et al.* 2019; Ji *et al.* 2020).

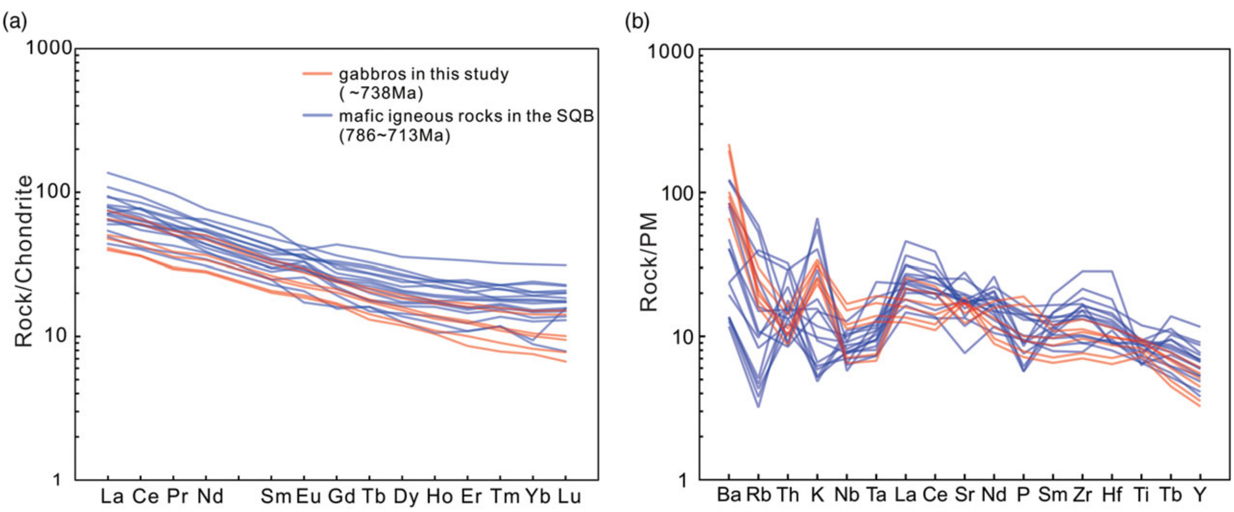

Fig. 5. (Colour online) (a) Chondrite-normalized REE patterns. (b) Primitive-mantle-normalized incompatible-element abundances. Chondrite and primitive-mantle values are from Sun & McDonough (1989).

https://doi.org/10.1017/S001675682200022X Published online by Cambridge University Press

Table 4. Hf-isotope compositions of zircon grains from the Xialanuoer gabbros

Spot	Age (Ma)	$^{176}Yb/^{177}Hf$	$^{176}Lu/^{177}Hf$	$^{176}Hf/^{177}Hf$	2σ	ϵ_{Hf} (*t*)	2σ	T_{DM} (Ma)	$T_{DM}{}^{C}$ (Ma)	$f_{Lu/Hf}$
DLH-1-2	730	0.036769	0.001260	0.282069	0.000050	−9.4	1.8	1679	2230	−0.96
DLH-1-3	725	0.050632	0.001627	0.282131	0.000031	−7.5	1.1	1607	2106	−0.95
DLH-1-4	1949	0.021780	0.000645	0.281546	0.000017	−0.7	0.6	2367	2620	−0.98
DLH-1-5	755	0.041887	0.001339	0.282146	0.000026	−6.2	0.9	1574	2046	−0.96
DLH-1-6	757	0.085620	0.002765	0.282037	0.000023	−10.7	0.8	1795	2331	−0.92
DLH-1-7	745	0.052945	0.001795	0.282025	0.000022	−10.9	0.8	1765	2335	−0.95
DLH-1-8	720	0.045595	0.001569	0.281954	0.000023	−13.8	0.8	1854	2498	−0.95
DLH-1-9	1295	0.039248	0.001187	0.281574	0.000018	−14.7	0.6	2362	2985	−0.96
DLH-1-10	2078	0.021172	0.000751	0.281411	0.000033	−2.8	1.2	2557	2845	−0.98
DLH-1-11	2397	0.011253	0.000439	0.281380	0.000037	3.8	1.3	2578	2690	−0.99

Table 5. Summary of published zircon U–Pb ages for the *ca.* 824–675 Ma magmatic rocks in the northeastern Tibetan Plateau

No.	Location	Rock type	Dating method*	Age (Ma)	Reference
1	North Qilian	Gneissic granites	LA-ICP-MS U–Pb	751 ± 14	Su *et al.* 2004
2	North Qilian	Gneissic granites	SHRIMP U–Pb	774 ± 23	Tseng *et al.* 2006
3	North Qilian	Gneissic granites	SHRIMP U–Pb	776 ± 10	Tseng *et al.* 2006
4	North Qilian	Gabbros	LA-ICP-MS U–Pb	675 ± 31	Song *et al.* 2016
5	North Qilian	Basalts	LA-ICP-MS U–Pb	764 ± 3	Song *et al.* 2016
6	North Qilian	Basalts	TIMS U–Pb	733 ± 7	Mao *et al.* 1997
7	North Qilian	Basalts	TIMS U–Pb	738 ± 4	Mao *et al.* 1997
8	South Qilian	Basalts	LA-ICP-MS U–Pb	786 ± 5	Ji *et al.* 2020
9	South Qilian	Basalts	LA-ICP-MS U–Pb	713 ± 4	Wang *et al.* 2019
10	South Qilian	Basalts	LA-ICP-MS U–Pb	736 ± 6	Bai *et al.* 2019
11	South Qilian	Trachytes	LA-ICP-MS U–Pb	740 ± 14	Bai *et al.* 2019
12	South Qilian	Gabbros	LA-ICP-MS U–Pb	730 ± 3	Ma *et al.* 2017
13	South Qilian	Gabbros	LA-ICP-MS U–Pb	738 ± 11	This study
14	North Qaidam	Gneissic granites	LA-ICP-MS U–Pb	744 ± 28	Lu *et al.* 2002
15	North Qaidam	Basalts	LA-ICP-MS U–Pb	768 ± 39	Yang *et al.* 2006
16	North Qaidam	Gabbros	LA-ICP-MS U–Pb	780 ± 22	Yang *et al.* 2006
17	North Qaidam	Basalts	LA-ICP-MS U–Pb	748 ± 6	Chen *et al.* 2009
18	North Qaidam	Basalts	LA-ICP-MS U–Pb	795 ± 7	Chen *et al.* 2009
19	East Kunlun	Diabases	LA-ICP-MS U–Pb	733 ± 6	Ren *et al.* 2010
20	East Kunlun	Gabbros	LA-ICP-MS U–Pb	796 ± 41	Ren *et al.* 2011
21	Central Qilian Block	Basalts	LA-ICP-MS U–Pb	713 ± 53	Xu *et al.* 2008
22	Central Qilian Block	Basalts	LA-ICP-MS U–Pb	824 ± 49	Xu *et al.* 2008
23	Quanji Block	Basaltic andesites	TIMS U–Pb	800	Li *et al.* 2003

* SHRIMP: sensitive high-resolution ion microprobe; TIMS: thermal ionization mass spectrometry.

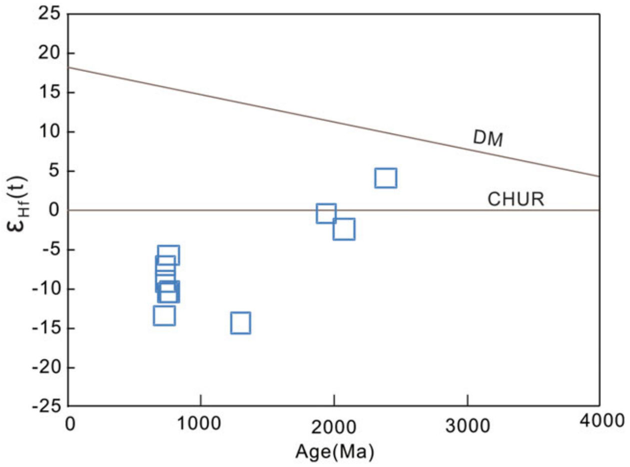

Fig. 6. (Colour online) Zircon Hf-isotope compositions of the Xialanuoer gabbros.

crustal contamination. In addition, their Lu/Yb ratios (0.14–0.15) are lower than those expected for continental crust (0.16–0.18) (Rudnick & Gao, 2003). Their Nb/Ta ratios (average of 15.85) are higher than crustal average values (12–13) (Barth *et al.* 2000) but closer to the values expected for the mantle (15.9 ± 0.6) (Pfänder *et al.* 2007), suggesting derivation from a parental magma generated by partial melting of mantle material that underwent insignificant crustal contamination prior to emplacement.

Asthenosphere–lithosphere interaction plays a key role in the genesis of continental basalts (Turner & Hawkesworth, 1995), and Nb/La ratios can be used to discriminate between magmas derived from the asthenospheric mantle and the sub-continental lithospheric mantle (SCLM). Asthenospheric mantle-derived melts are generally characterized by high Nb/La ratios (0.9–1.3) (Sun & McDonough, 1989), whereas SCLM-derived melts have lower Nb/La ratios that are similar to those expected for continental crust (Wang *et al.* 2014). The Xialanuoer gabbros have low Nb/La ratios (average of 0.72) that are similar to those expected for SCLM-derived melts (Wang *et al.* 2014), and their low Th/Nb and Th/La ratios (averages of 0.12 and 0.08, respectively) are consistent with derivation from enriched mantle of type-I (EMI-type) mantle (Saunders *et al.* 1987; Weaver, 1991; Ernst & Buchan, 2003). Combining the very negative zircon $\epsilon_{Hf}(t)$ values (−13.8 to −6.2) with the trace element geochemical characteristics of the Xialanuoer gabbros suggests that they probably formed from melts derived from an EMI-type enriched region of the lithospheric mantle.

6.c. Tectonic setting

The tectonic setting of the Mid-Neoproterozoic magmatic activity in the SQB remains controversial, with some studies suggesting this magmatism occurred in a continental rift setting (Bai *et al.* 2019; Ji *et al.* 2020) and others inferring that it occurred in an active continental arc setting (Ma *et al.* 2017; Wang *et al.* 2019).

Arc-type and within-plate basalts can be distinguished using Zr/Sm and Ti/V ratios (Zhou *et al.* 2007). In general, within-plate basalts have high Zr/Sm (>25) and Ti/V ratios (>20). The majority of the Xialanuoer gabbros and contemporaneous mafic rocks in the SQB have high Zr/Sm (25–38) and Ti/V (24–56) ratios (Ma *et al.* 2017; Bai *et al.* 2019; Wang *et al.* 2019; Ji *et al.* 2020) that are consistent with the values expected for within-plate basalts. Continental rift basalts have Th/Ta and Ta/Hf values of 1.6–4.0 and 0.1–0.3, respectively (Wang *et al.* 2001). The Xialanuoer gabbros and contemporaneous mafic rocks have Th/Ta and Ta/Hf ratios of 1.66–to 3.65 and 0.09–0.28, respectively (Ma *et al.* 2017; Bai *et al.* 2019; Wang *et al.* 2019; Ji *et al.* 2020), indicative of formation in a continental rift setting. Plotting the Xialanuoer gabbros and mafic rocks on Zr vs Zr/Y, Zr vs TiO_2, Ti/100 – Zr – Y * 3, and Nb * 2 – Zr/4 – Y diagrams yields similar results (Fig. 7a–d).

The 796–675 Ma mafic rocks in the northeastern Tibetan Plateau formed in a within-plate setting (Fig. 7a–d), again consistent with a continental rift setting (Xu *et al.* 2008; Chen *et al.* 2009; Ren *et al.* 2010, 2011; Song *et al.* 2016; Xia *et al.* 2016; Ma *et al.* 2017; Bai *et al.* 2019; Ji *et al.* 2020). The Mid-Neoproterozoic magmatism in the SQB therefore represents an extension of the magmatism identified in the Quanji and Central Qilian blocks. This ~600 km long igneous belt extends from the northwestern and central parts of the SQB to the southeastern SQB, through the western Danghenanshan and on to eastern Tianjun (Fig. 1b).

6.d. Tectonic implication

The Xialanuoer gabbros provide further constraints on the composition of Precambrian basement rocks in the SQB and the crustal evolution of this region. The captured *ca.* 2397 and 2078–1295 Ma zircon grains in the gabbro have one positive $\epsilon_{Hf}(t)$ (+3.8) and multiple negative (−14.7 to −0.7) $\epsilon_{Hf}(t)$ values, respectively (Table 4; Fig. 6), indicating the probable existence of Early Precambrian basement rocks in the SQB and providing evidence of Palaeoproterozoic crustal growth and Mesoproterozoic reworking.

Previous studies have indicated that the Central Qilian Block and surrounding terranes were involved in the Neoproterozoic amalgamation and break-up of Rodinia (Song *et al.* 2013; Tung *et al.* 2013; Xu *et al.* 2015; Yan *et al.* 2015; Wang *et al.* 2017; Zhang *et al.* 2017; S Li *et al.* 2018; Qin *et al.* 2018), an event associated with magmatism (Table 5). These continental rift-related magmatic rocks are widespread in the Qilian – Qaidam – East Kunlun region of the northeastern Tibetan Plateau and record the lithospheric extension and thinning. The Duoruonuoer Group in the Central Qilian Block, the schists of the Balonggonggaer Formation in the SQB, and the Heitupo-Hongtiegou-Zhoujieshan Formations of the Quanji Group in the Quanji Block provide the sedimentary record of Mid-Neoproterozoic continental rifting within the northeastern Tibetan Plateau (Li *et al.* 2003; Ji *et al.* 2018; Qin, 2018; Li *et al.* 2019).

Widespread Mid-Neoproterozoic continental rift-type sedimentation and anorogenic magmatism is also recorded in other Rodinia blocks, including the Tarim (Xu *et al.* 2013; Zhang *et al.* 2013), South China (Ling *et al.* 2003; Wang *et al.* 2011; Wan *et al.* 2019), Australia (Powell *et al.* 1994; Wingate *et al.* 1998; Preiss, 2000), North America (Park *et al.* 1995; McClellan & Gazel, 2014) and Southern Africa blocks (Frimmel *et al.* 2001). These major global rifting events triggered Rodinian disintegration.

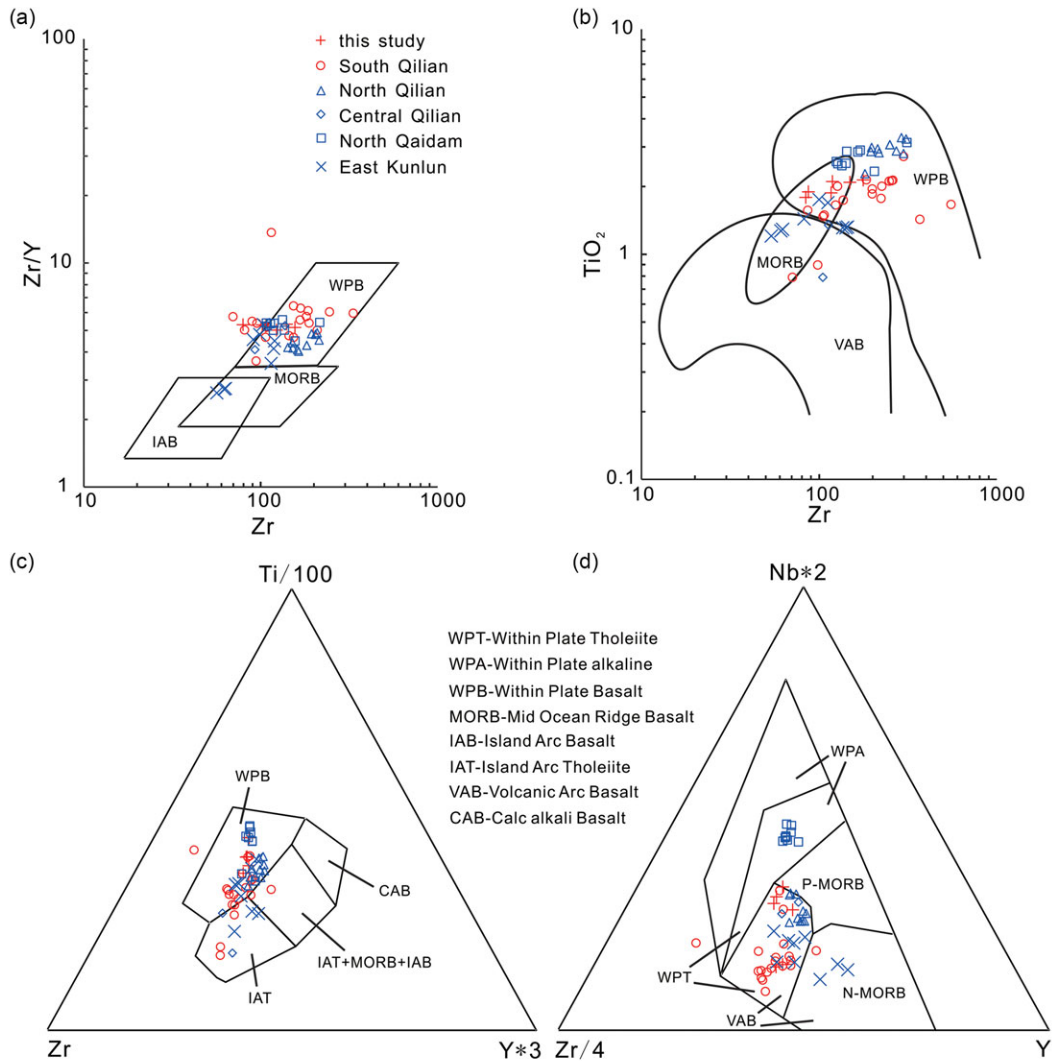

Fig. 7. (Colour online) Mid-Neoproterozoic gabbros in this study and 796–675 Ma mafic igneous rocks from the South Qilian (Ma *et al*. 2017; Bai *et al*. 2019; Wang *et al*. 2019; Ji *et al*. 2020), North Qilian (Mao *et al*. 1997; Song *et al*. 2016), Central Qilian (Xu *et al*. 2008), North Qaidam (Chen *et al*. 2009) and East Kunlun regions (Ren *et al*. 2010, 2011), plotted in the (a) Zr vs Zr/Y, (b) Zr vs TiO_2 (Pearce & Norry, 1979), (c) Ti/100 − Zr − Y * 3 (Pearce & Cann, 1973) and (d) Nb * 2 − Zr/4 − Y tectonic discrimination diagrams (Meschede, 1986).

7. Conclusions

(1) The Xialanuoer gabbros in the SQB formed at *ca.* 738 Ma, and was contemporaneous with the widespread mafic magmatism in the northeastern Tibetan Plateau.
(2) The Xialanuoer gabbros underwent little to no crustal contamination and show geochemical characteristics of within-plate basalts. Their parental magma was probably sourced from an EMI-type enriched region of the lithospheric mantle. They formed in a continental rift setting, rather than an arc-related setting.
(3) In the SQB, crustal growth and reworking likely occurred in the Palaeoproterozoic and Mesoproterozoic.
(4) The Central Qilian, Quanji, Qaidam and East Kunlun blocks that make up the present northeastern Tibetan Plateau played a significant role during the break-up of Rodinia.

Notes.

Acknowledgements. We are very grateful to editor-in-chief Prof. Peter Clift, Prof. Fernando Corfu, Prof. Frederico Castro Jobim Vilalva and Prof. Qian Liu for their constructive suggestions and comments, which led to significant improvement of the manuscript. We would also like to thank Mr ShaoYi Ban for his assistance during the field work, and Mr Huadong Gong for laboratory assistance. This research was jointly supported by the National Science and Technology Major Project (No. 2016ZX05003006), the Natural Science Foundation of Shaanxi Province, China (No. 2021JQ-630 and 2021JQ-631), the Youth Fund of Shandong Bureau of China Metallurgical Geology Bureau (No. SDYJ-QNKY202004), the Doctoral Research Startup Project of Yan'an University (No. YDBK2019-68 and YDBK2019-69), and the Innovation and Entrepreneurship training programme project for undergraduates of Yan'an University (No. D2020121 and D2020122).

Declaration of interest. The authors declare that they have no conflicts of interest.

References

Albarède F, Scherer EE, Blichert-Toft J, Rosing M, Simionovici A and Bizzarro M (2006) γ-ray irradiation in the early Solar System and the conundrum of the ^{176}Lu decay constant. *Geochimica et Cosmochimica Acta* **70**, 1261–70.

Andersen T (2002) Correction of common lead in U-Pb analyses that do not report ^{204}Pb. *Chemical Geology* **192**, 59–79.

Bai CD, Zhuan SP, Mao ZF, Chen YY and Li J (2019) LA-ICP-MS zircon U-Pb ages, geochemical characteristics and geotectonic significance of the metamorphosed volcanic rocks in Neoproterozoic Balongonggaer formation in Tianjun County, Southern Qilian mountain. *Geological Review* **65**, 756–71.

Barth MG, McDonough WF and Rudnick RL (2000) Tracking the budget of Nb and Ta in the continental crust. *Chemical Geology* **165**, 197–213.

BGMRQH (1997) *Regional Geology of Qinghai Province (Bureau of Geology and Mineral Resources of Qinghai Province).* Beijing: Geological Publishing House, 300 pp.

Bienvenu P, Bougault H, Joron JL, Treuil M and Dmitriev L (1990) MORB alteration: rare-earth element/non-rare-earth hygromagmaphile element fractionation. *Chemical Geology* **82**, 1–14.

Bouvier A, Vervoort JD and Patchett PJ (2008) The Lu-Hf and Sm-Nd isotopic composition of CHUR: constraints from unequilibrated chondrites and implications for the bulk composition of terrestrial planets. *Earth and Planetary Science Letters* **273**, 48–57.

Chen DL, Liu L, Sun Y and Liou JG (2009) Geochemistry and zircon U-Pb dating and its implications of the Yukahe HP/UHP terrane, the North Qaidam, NW China. *Journal of Asian Earth Sciences* **35**, 259–72.

Chu NC, Taylor RN, Chavagnac V, Nesbitt RW, Boella RM, Milton JA, German CR, Bayon G and Burton K (2002) Hf isotope ratio analysis using multi-collector inductively coupled plasma mass spectrometry: an evaluation of isobaric interference corrections. *Journal of Analytical Atomic Spectrometry* **17**, 1567–74.

Corfu F, Hanchar JM, Hoskin PWO and Kinny P (2003) Atlas of zircon textures. *Reviews in Mineralogy and Geochemistry* **53**, 469–500.

Ernst RE and Buchan KL (2003) Recognizing mantle plumes in the geological record. *Earth and Planetary Science Letters* **31**, 469–523.

Frimmel HE, Zartman RE and Späth A (2001) The Richtersveld igneous complex, South Africa: U-Pb zircon and geochemical evidence for the beginning of Neoproterozoic continental breakup. *Journal of Geology* **109**, 493–508.

Fu CL, Yan Z, Wang ZQ, Buckman S, Aitchison JC, Niu ML, Cao B, Guo XQ, Li X, Li Y and Li J (2018) Lajishankou ophiolite complex: implications for paleozoic multiple accretionary and collisional events in the South Qilian Belt. *Tectonics* **37**, 1321–46.

Griffin WL, Pearson NJ, Belousova E, Jackson SE, Van Achterbergh E, O'Reilly SY and Shee SR (2000) The Hf isotope composition of cratonic mantle: LAM-MC-ICPMS analysis of zircon megacrysts in kimberlites. *Geochimica et Cosmochimica Acta* **64**, 133–47.

Griffin WL, Wang X, Jackson SE, Pearson NJ and O'Reilly SY (2002) Zircon geochemistry and magma mixing, SE China: in-situ analysis of Hf isotopes, Tonglu and Pingtan igneous complexes. *Lithos* **61**, 237–69.

Günther D and Hattendorf B (2005) Solid sample analysis using laser ablation inductively coupled plasma mass spectrometry. TrAC – *Trends in Analytical Chemistry* **24**, 255–65.

Hou QY, Zhang HF, Zhang BR, Zhao ZD and Zhu YH (2005) Pb and Nd isotopic compositions of basement and granitoid in the Qilianshan: constraints on tectonic affinity. *Earth Science – Journal of China University of Geosciences* **30**, 62–70.

Jenner GA, Foley SF, Jackson SE, Green TH, Fryer BJ and Longerich HP (1993) Determination of partition coefficients for trace elements in high pressure-temperature experimental run products by laser ablation microprobe-inductively coupled plasma-mass spectrometry (LAM-ICP-MS). *Geochimica et Cosmochimica Acta* **57**, 5099–103.

Ji B, Li X, Huang B, Wang L and Wang G (2020) Zircon U-Pb dating and geochemistry of basalt in Guaizhangshan group from the southern Danghe mountains in south Qilian and its tectonic setting. *Geology in China* **25**, 1–21.

Ji B, Yu J, Li X, Huang B and Wang L (2018) The disintegration of Balonggongge'er formation and the definition of lithostratigraphic unit in Danghenanshan area of South Qilian mountain: evidence from petrology and chronology. *Geological Bulletin of China* **37**, 621–33.

Li DL, Sun DL, Zhao ZY, Sun J, Yang ZZ, Tian Z, Li XM and Yang BZ (2018) A discussion on the geological characteristics and formation time of Balonggongga'er formation in Xiawu area of Qinghai province. *Geological Bulletin of China* **37**, 635–41.

Li HK, Lu SN, Wang HC, Xiang ZQ and Zhen JK (2003) Geochronological framework of the Neoproterozoic major geological events in the northern margin of the Qaidam basin. *Geological Survey and Research* **26**, 28–37.

Li M, Wang C, Li R, Meert Jg, Peng Y and Zhang J (2019) Identifying late Neoproterozoic–early Paleozoic sediments in the South Qilian Belt, China: a peri-Gondwana connection in the northern Tibetan Plateau. *Gondwana Research* **76**, 173–84.

Li S, Zhao S, Liu X, Cao H, Yu S, Li X, Somerville I, Yu S and Suo Y (2018) Closure of the Proto-Tethys ocean and early Paleozoic amalgamation of microcontinental blocks in East Asia. *Earth-Science Reviews* **186**, 37–75.

Li ZX, Bogdanova SV, Collins AS, Davidson A, De Waele B, Ernst RE, Fitzsimons ICW, Fuck RA, Gladkochub DP, Jacobs J, Karlstrom KE, Lu S, Natapov LM, Pease V, Pisarevsky SA, Thrane K and Vernikovsky V (2008) Assembly, configuration, and break-up history of Rodinia: a synthesis. *Precambrian Research* **160**, 179–210.

Liao H, Hu DG, Zhang XJ, Yu WL and Guo T (2014) Zircon U-Pb age for granite of the Ordovician formation and its tectonic significance in the southern Qilian. *Journal of Geomechanics* **20**, 293–8.

Ling W, Gao S, Zhang B, Li H, Liu Y and Cheng J (2003) Neoproterozoic tectonic evolution of the northwestern Yangtze Craton, South China: implications for amalgamation and break-up of the Rodinia Supercontinent. *Precambrian Research* **122**, 111–40.

Liu XM, Gao S, Diwu CR, Yuan HL and Hu ZC (2007) Simultaneous in-situ determination of U-Pb age and trace elements in zircon by LA-ICP-MS in 20 μm spot size. *Chinese Science Bulletin* **52**, 1257–64.

Liu Y, Liu XM, Hu ZC, Diwu CR, Yuan HL and Gao S (2007) Evaluation of accuracy and long-term stability of determination of 37 trace elements in geological samples by ICP-MS. *Acta Petrologica Sinica* 23, 1203–10.

Lu S, Li H, Zhang C and Niu G (2008) Geological and geochronological evidence for the Precambrian evolution of the Tarim Craton and surrounding continental fragments. *Precambrian Research* **160**, 94–107.

Lu SN, Yu HF, Jin W, Li HK and Zhen JK (2002) Microcontinents on the eastern margin of Tarim paleocontinent. *Acta Petrologica et Mineralogica* **21**, 318–26.

Ludwig K (2003) *ISOPLOT 3.0: A Geochronological Toolkit for Microsoft Excel.* Berkeley, California: Berkeley Geochronology Center.

Ma W, Jia JT, Li WF, Ma YJ, Lei XQ, Ren EF and Xu B (2017) LA-ICP-MS zircon U-Pb age of gabbro from Yangkang area in South Qilian and its geological significance. *Northwestern Geology* **50**, 75–82.

Mao J, Zhang Z, Yang J, Song B, Wu M and Zuo G (1997) Dating of single-grain zircon for Precambrian strata in western part of North Qilian Mountains. *Chinese Science Bulletin* **42**, 1414–17.

McClellan E and Gazel E (2014) The Cryogenian intra-continental rifting of Rodinia: evidence from the Laurentian margin in eastern North America. *Lithos* **206–207**, 321–37.

Meschede M (1986) A method of discriminating between different types of mid-ocean ridge basalts and continental tholeiites with the Nb-Zr-Y diagram. *Chemical Geology* **56**, 207–18.

Niu GZ, Huang G, Deng CS, Xu Y, Chen T, Ji C and Li WJ (2016) LA-ICP-MS zircon U-Pb ages of metamorphic volcanic rocks in Balonggongge'er formation of South Qilian mountain in Qinghai province and their geological significance. *Geological Bulletin of China* **35**, 1442–7.

Park JK, Buchan KL and Harlan SS (1995) A proposed giant radiating dyke swarm fragmented by the separation of Laurentia and Australia based on paleomagnetism of ca. 780 Ma mafic intrusions in western North America. *Earth and Planetary Science Letters* **132**, 129–39.

Pearce JA (1982) Trace element characteristics of lavas from destructive plate boundaries. In *Andesites: Orogenic Andesites and Related Rocks* (ed RS Thorpe), pp. 525–48. New York: Wiley.

Pearce JA and Cann JR (1973) Tectonic setting of basic volcanic rocks determined using trace element analyses. *Earth and Planetary Science Letters* **19**, 290–300.

Pearce JA and Norry MJ (1979) Petrogenetic implications of Ti, Zr, Y, and Nb variations in volcanic rocks. *Contributions to Mineralogy and Petrology* **69**, 33–47.

Peng Y, Yu S, Li S, Zhang J, Liu Y, Li Y and Santosh M (2019) Early Neoproterozoic magmatic imprints in the Altun-Qilian-Kunlun region of the Qinghai-Tibet Plateau: response to the assembly and breakup of Rodinia supercontinent. *Earth-Science Reviews* **199**, 102954.

Pfänder JA, Münker C, Stracke A and Mezger K (2007) Nb/Ta and Zr/Hf in ocean island basalts: implications for crust-mantle differentiation and the fate of Niobium. *Earth and Planetary Science Letters* **254**, 158–72.

Powell CMA, Preiss WV, Gatehouse CG, Krapez B and Li ZX (1994) South Australian record of a Rodinian epicontinental basin and its mid-

Neoproterozoic breakup (~700 Ma) to form the Palaeo-Pacific Ocean. *Tectonophysics* **237**, 113–40.

Preiss WV (2000) The Adelaide geosyncline of south Australia and its significance in Neoproterozoic continental reconstruction. *Precambrian Research* **100**, 21–63.

Qin Y (2018) Neoproterozoic to Early Paleozoic Tectonic Evolution in the South Qilian Orogen. Xi'an: Northwest University, 153 pp.

Qin Y, Feng Q, Chen G, Chen Y, Zou KZ, Liu Q, Jiao QQ, Zhou DW, Pan LH and Gao JD (2018) Devonian post-orogenic extension-related volcano-sedimentary rocks in the northern margin of the Tibetan Plateau, NW China: implications for the Paleozoic tectonic transition in the North Qaidam Orogen. *Journal of Asian Earth Sciences* **156**, 145–66.

Qin Y, Zhang XL, Feng Q, Zhang X, Gao JD and Chen Y (2021) Paleozoic tectonic transition of the North Qilian Belt in the northern margin of the Tibetan Plateau, NW China: insights from detrital zircon U-Pb geochronology and sedimentology. *Geological Journal* **56**, 5531–49.

Ren JH, Liu YQ, Zhou DW, Feng Q, Zhang K, Dong ZL and Qin PL (2010) Geochemical characteristics and LA-ICP-MS zircon U-Pb dating of basic dykes in the Xiaomiao area, Eastern Kunlun. *Journal of Jilin University* **40**, 860–8.

Ren JH, Zhang K, Liu YQ, Zhou DW and Feng Q (2011) Geochemical characteristics and zircon dating of basalt-gabbro from the South Jinshuikou area, Eastern Kunlun. *Journal of Northwest University* **41**, 101–6.

Rubatto D (2002) Zircon trace element geochemistry: partitioning with garnet and the link between U-Pb ages and metamorphism. *Chemical Geology* **184**, 123–38.

Rudnick RL and Gao S (2003) *Composition of the Continental Crust.* Amsterdam: Elsevier Inc.

Saunders AD, Rogers G, Marriner GF, Terrell DJ and Verma SP (1987) Geochemistry of Cenezoic volcanic rocks, Baja California, Mexico: implications for the petrogenesis of post-subduction magmas. *Journal of Volcanology and Geothermal Research* **32**, 223–45.

Song SG, Niu YL, Su L and Xia XH (2013) Tectonics of the North Qilian orogen, NW China. *Gondwana Research* **23**, 1378–401.

Song TZ, Liu JD, Li J, Zhang XY, Liang KX and Zhen Y (2016) LA-ICP-MS zircon U-Pb age of gabbro and basalt in the Baimuxia area of North Qilian and its geological significance. *Northwestern Geology* **49**, 33–42.

Su JP, Hu NG, Zhang HF and Fu GM (2004) Single zircon U-Pb dating and geological significance of the Diaodaban western segment of Northern Qilian Mountain. *Geological Science and Technology Information* **23**, 12–14.

Sun SS and McDonough WF (1989) Chemical and isotopic systematics of oceanic basalts: implications for mantle composition and processes. In *Magmatism in the Ocean Basins* (eds AD Saunders and MJ Norry), pp. 313–45. *Geological Society of London, Special Publication* no. 42.

Tseng CY, Yang HY, Wan Y, Liu D, Wen DJ, Lin TC and Tung KA (2006) Finding of Neoproterozoic (~775 Ma) magmatism recorded in metamorphic complexes from the North Qilian orogen: evidence from SHRIMP zircon U-Pb dating. *Chinese Science Bulletin* **51**, 963–70.

Tung KA, Yang HY, Liu DY, Zhang JX, Yang HJ, Shau YH and Tseng CY (2013) The Neoproterozoic granitoids from the Qilian block, NW China: evidence for a link between the Qilian and South China blocks. *Precambrian Research* **235**, 163–89.

Turner S and Hawkesworth C (1995) The nature of the sub-continental mantle: constraints from the major-element composition of continental flood basalts. *Chemical Geology* **120**, 295–314.

Wan L, Zeng Z, Asimow PD, Zeng Z, Peng L, Xu D, Wei Y, Liu W, Lu C and Chang W (2019) Mid-Neoproterozoic mafic rocks in the western Jiangnan orogen, South China: intracontinental rifting or subduction? *Journal of Asian Earth Sciences* **185**, 104039.

Wang L, Li XM, Hu ZG, Yang C, Guo LF, Yan HZ, Ge RC and Ji B (2019) Zircon U-Pb dating and geochemistry of Kebasitao basalt from the middle part of southern Danghe mountains in Southern Qilian and its geological implication. *Geotectonica et Metallogenia* **43**, 1069–77.

Wang R, Xu Z, Santosh M, Xu X, Deng Q and Fu X (2017) Middle Neoproterozoic (ca. 705–716 Ma) arc to rift transitional magmatism in the northern margin of the Yangtze block: constraints from geochemistry, zircon U–Pb geochronology and Hf isotopes. *Journal of Geodynamics* **109**, 59–74.

Wang XC, Li ZX, Li J, Pisarevsky SA and Wingate MTD (2014) Genesis of the 1.21 Ga Marnda Moorn large igneous province by plume-lithosphere interaction. *Precambrian Research* **241**, 85–103.

Wang XC, Li ZX, Li XH, Li QL and Zhang QR (2011) Geochemical and Hf-Nd isotope data of Nanhua rift sedimentary and volcaniclastic rocks indicate a Neoproterozoic continental flood basalt provenance. *Lithos* **127**, 427–40.

Wang YL, Zhang CJ and Xiu SZ (2001) Th/Hf-Ta/Hf identification of tectonic setting of basalts. *Acta Petrologica Sinica* **17**, 414–21.

Weaver BL (1991) The origin of ocean island basalt end-member compositions: trace element and isotopic constraints. *Earth and Planetary Science Letters* **104**, 381–97.

Wiedenbeck M, Allé P, Corfu F, Griffin WL, Meier M, Oberli F, Von Quadt A, Roddick JC and Spiegel W (1995) Three natural zircon standards for U-Th-Pb, Lu-Hf, trace element and REE analyses. *Geostandards Newsletter* **19**, 1–23.

Wilson M (1989) *Igneous Petrogenesis.* Dordrecht: Springer.

Winchester JA and Floyd PA (1977) Geochemical discrimination of different magma series and their differentiation products using immobile elements. *Chemical Geology* **20**, 325–43.

Wingate MTD, Campbell IH, Compston W and Gibson GM (1998) Ion microprobe U-Pb ages for Neoproterozoic basaltic magmatism in south-central Australia and implications for the breakup of Rodinia. *Precambrian Research* **87**, 135–59.

Wu FY, Yang YH, Xie LW, Yang JH and Xu P (2006) Hf isotopic compositions of the standard zircons and baddeleyites used in U-Pb geochronology. *Chemical Geology* **234**, 105–26.

Xia LQ, Li XM, Yu JY and Wang GQ (2016) Mid-late Neoproterozoic to early Paleozoic volcanism and tectonic evolution of the Qilianshan, NW China. *GeoResJ* **9–12**, 1–41.

Xiao WJ, Windley BF, Yong Y, Yan Z, Yuan C, Liu CZ and Li JL (2009) Early Paleozoic to Devonian multiple-accretionary model for the Qilian Shan, NW China. *Journal of Asian Earth Sciences* **35**, 323–33.

Xu WC, Zhang HF and Liu XM (2007) U-Pb zircon dating constraints on formation time of Qilian high-grade metamorphic rock and its tectonic implications. *Chinese Science Bulletin* **52**, 531–8.

Xu X, Song SG, Su L, Li ZX, Niu YL and Allen MB (2015) The 600–580 Ma continental rift basalts in North Qilian Shan, northwest China: links between the Qilian-Qaidam block and SE Australia, and the reconstruction of East Gondwana. *Precambrian Research* **257**, 47–64.

Xu XY, Wang HL, Chen JL, He SP, Wu P and Gao T (2008) Zircon U-Pb dating and petrogenesis of Xinglongshan group basic volcanic rocks at eastern segment of Middle Qilian Mts. *Acta Petrologica Sinica* 24, 827–40.

Xu YJ, Du YS, Cawood PA, Guo H, Huang H and An ZH (2010) Detrital zircon record of continental collision: assembly of the Qilian Orogen, China. *Sedimentary Geology* **230**, 35–45.

Xu ZQ, He BZ, Zhang CL, Zhang JX, Wang ZM and Cai ZH (2013) Tectonic framework and crustal evolution of the Precambrian basement of the Tarim Block in NW China: new geochronological evidence from deep drilling samples. *Precambrian Research* **235**, 150–62.

Yan Z, Aitchison J, Fu C, Guo X, Niu M, Xia W and Li J (2015) Hualong complex, South Qilian terrane: U-Pb and Lu-Hf constraints on Neoproterozoic micro-continental fragments accreted to the northern Proto-Tethyan margin. *Precambrian Research* **266**, 65–85.

Yan Z, Fu CL, Aitchison J, Niu M, Buckman S and Cao B (2019) Early Cambrian Muli arc–ophiolite complex: a relic of the Proto-Tethys oceanic lithosphere in the Qilian Orogen, NW China. *International Journal of Earth Sciences* **108**, 1147–64.

Yang JH, Du YS, Cawood PA and Xu YJ (2009) Silurian collisional suturing onto the southern margin of the North China craton: detrital zircon geochronology constraints from the Qilian Orogen. *Sedimentary Geology* **220**, 95–104.

Yang JS, Wu CL, Zhang JX, Shi RD, Meng FC, Wooden J and Yang HY (2006) Protolith of eclogites in the north Qaidam and Altun UHP terrane, NW China: earlier oceanic crust? *Journal of Asian Earth Sciences* **28**, 185–204.

Yu SY, Zhang JX, Qin HP, Sun DY, Zhao XL, Cong F and Li YS (2015) Petrogenesis of the early Paleozoic low-Mg and high-Mg adakitic rocks in the North Qilian orogenic belt, NW China: implications for transition from crustal thickening to extension thinning. *Journal of Asian Earth Sciences* **107**, 122–39.

Zhang CL, Zou HB, Li HK and Wang HY (2013) Tectonic framework and evolution of the Tarim block in NW China. *Gondwana Research* **23**, 1306–15.

Zhang GD, Xu ZQ, Gong J, Fen J, Han YB, Zhang JW, Zhou Y and Huang Z (2016) Geochronology and significance of intermediate-acid intrusive rocks in Quanji area, Gangcha, Qinghai. *Geological Journal of China Universities* 22, 113–26.

Zhang YQ, Song SG, Yang LM, Su L, Niu YL, Allen MB and Xu X (2017) Basalts and picrites from a plume-type ophiolite in the South Qilian accretionary belt, Qilian Orogen: accretion of a Cambrian oceanic plateau? *Lithos* **278–281**, 97–110.

Zhou J, Li XH, Ge W and Li ZX (2007) Age and origin of middle Neoproterozoic mafic magmatism in southern Yangtze block and relevance to the break-up of Rodinia. *Gondwana Research* **12**, 184–97.